TECHNICAL ARTICLE

Coaxial Laser Cladding of Cobalt-Base Alloy Stellite™ 6 on Grey Cast Iron Analysis of the Microstructural and Mechanical Properties Depending on the Laser Power

Maximilian Kiehl, Adriano Scheid, Karin Graf, Benedikt Ernst, and Ulrich Tetzlaff

A high-power diode laser was used to generate single- and multi-bead coatings of Stellite™ 6 by coaxial laser cladding over flat grey cast iron (EN-GJLP-200) as a preliminary study to develop a wear and corrosion resistant coating for brake disks on a cost-effective substrate. In this article, we have focused on a detailed quantitative analysis of the effect of different laser powers (1.5, 2.0, 2.5, 3.0, 3.5, and 4.0 kW) on the bead geometry, dilution, microstructure, and hardness. Coatings dilution or composition depends directly on the laser power as well as bead geometry. The typical microstructure of the coatings comprises a solid solution of α (hcp)- and β (fcc)-Co with a dendritic structure as a metal matrix and an interdendritic lamellar eutectic, which contains predominantly β-Co, chromium carbides Cr_7C_3 and $Cr_{23}C_6$ as well as blocky tungsten carbide W_2C. Coating hardness depends on the chemical composition and microstructure that is modified by the deposition parameters. Low laser power results in high carbide fraction and most refined microstructures, accounting for harder coatings.

1. Introduction

Co-based hardfacing alloys like Stellite™ 6 are used in surface engineering for applications requiring outstanding sliding wear, oxidation, and corrosion resistance during service at elevated temperatures such as under aggressive operating conditions in the petrochemistry, nuclear reactors or food processing facilities (Ref 1-6). The application of Stellite™ 6 involves huge cost and laser surface cladding may be a viable option for its cost-effective utilization to extend the functionality and performance limit of conventionally used grey cast iron (EN-GJLP-200) as brake disk in mechanical protection (friction, wear), barrier function (corrosion resistance), and optical properties (reflection, absorption) (Ref 3, 6-8).

Co-28Cr-4.5W-1.2C wt.% are the main constituents of Stellite™ 6 in which Cr provides corrosion resistance while carbides add strength (Ref 9). The refractory metals, Mo and W are solid solution hardening elements (Ref 7), while the content of C contributes to the strength via precipitation hardening by forming carbides and intermetallic phases (Ref 5). For a C content lower than 2 wt.%, the first phase of the microstructure to form is dendritic β-Co with a metastable face-centered cubic

(fcc) crystal lattice at ambient temperature (Ref 5). The remaining liquid solidifies by a eutectic reaction into an interdendritic lamellar mixture of β-Co and Cr rich carbides, depending on alloy composition and laser cladding process parameters (Ref 2, 10).

Work carried out on the laser cladding of Stellite™ 6 so far has been focused on the effects of laser processing parameters on the clad geometry, evolution of microstructure, hardness, and wear resistance with steel as substrate (Ref 1-7). Sun et al. and Alimardani et al. have investigated the effects of various parameters such as the laser energy, powder feed rate, and the number of laser tracks on the clad geometry and dilution of single tracks. It was shown that the clad height and depth of penetration zone into the substrate increase with laser energy, pulse frequency, and percentage overlapping (Ref 11, 12). The choice of low heat input (low dilution) has shown a processing disadvantage for protective surfaces since a correspondingly higher wettability angle and a smaller bead width increase the required number of weld beads and reduces the surface quality (Ref 13-15).

Frenk et al. investigated the solidification characteristics, the type, size, and the fraction of phases in laser tracks by changing the laser scan speed (Ref 16, 17). A similar study on the effect of interaction time during laser cladding demonstrated a finer microstructure with less dilution and high hardness in a short interaction time (Ref 18). Van Mol Otterloo et al. carried out a detailed TEM investigation and identified three different mechanisms namely solid solution hardening by W and Cr, dislocation interactions as well as dispersed metal carbides like M_7C_3, $M_{23}C_6$, and Co_3W (Ref 19). The hardness of the alloy was shown to be dependent on the microstructure and size of the dendrites, too (Ref 20). Multilayer cladding of Stellite™ 6 has been performed to create a microstructural gradient coating, that revealed alternate fine and coarse microstructures, which resulted in non-uniform hardness across the clad (Ref 21).

Maximilian Kiehl, Benedikt Ernst, and **Ulrich Tetzlaff**, Technische Hochschule Ingolstadt, Esplanade 10, 85049 Ingolstadt, Germany; and **Adriano Scheid** and **Karin Graf**, Universidade Federal do Paraná, Curitiba, PR 88060-000, Brazil. Contact e-mail: kiehl.maximilian @web.de.

This study focuses on the qualification of applicable laser powers for the construction of a wear and corrosion resistant coating of Stellite™ 6 for grey cast iron (EN-GJLP-200) as brake disk, since there is only a small amount of research work on this material combination so far. For this purpose, a characterization of single-beads (SB) and multi-beads (MB) of Stellite™ 6 particularly, geometry, dilution, microstructure, and hardness have been highlighted given the change in laser power.

2. Materials and Experimental Procedure

2.1 Substrate and Coating

Stellite™ 6 powder in spherical form as additive material with particle size range between 50 and 150 μm was deposited on sandblasted EN-GJLP-200 grey cast iron plates cleaned with acetone and dimension of $120 \times 120 \times 20$ mm^3 (Table 1).

2.2 Process Setup

The experimental setup used for this work consists of a high-power diode laser (HPDL) of type SL8600 (co. Preco Inc.) connected to a three-axis CNC table as a positioning device and a powder feeder with a mechanical wheel as a transport unit. Considering previous studies, the process parameter laser power L_P, travel speed v, focal distance d_F, laser spot size d_L, shielding gas flow $\dot{V}_{SG}$, nozzle angle α_N, feeding rate $\dot{m}_P$ and forming gas flow $\dot{V}_{FG}$ were chosen (Table 2) (Ref 4-8, 13-15, 22). Single- and multi-beads were deposited on an 80 mm straight path with the substrate initially at room temperature. The laser powers from 1.5 to 4.0 kW in 0.5 kW increments are used for single-beads and 1.5 to 2.0 kW for multi-beads. The multi-beads are produced with a continuous zigzag pattern in the y-direction and an overlap φ of 30%.

2.3 Microstructural Investigations

2.3.1 Determination of Chemical Composition. The optical emission spectrometer (OES) SpectroMAX (co. SPEC-TRO Analytical Instruments GmbH) was used to determine the chemical composition of the substrate material EN-GJLP-200. The Fe content of the multi-beads was quantified with the x-ray fluorescence spectroscopy (XRF) analyzer Niton XL2-air (co. analyticon instruments GmbH).

2.3.2 Metallographic Preparation. First, the specimens were removed from the coated substrate plates by wire erosion or sawing. Afterward, the embedded cross sections were prepared by grinding and polishing using the following process: 120 and 220 SiC paper with water, 9 and 6 μm diamant discs with alcohol-based diamond lubricant, and cloth with 0.06 μm SiC suspension. The specimens were etched additionally in alcoholic 3 wt.% nitric acid (HNO$_3$). For investigations with EBSD, vibration polishing was carried out on an ATM Saphir Vibro (co. ATM GmbH) with the following parameters: Iota polishing cloth, Eposil M-11 suspension, 90 Hz vibration frequency, 90 g rear weight per specimen, and a duration of 13 min.

2.3.3 Optical Microscopy. The reflecting microscope HCL3TP (co. Leica GmbH) was used for a characterization of the geometry of single-beads including the reinforced height h_R, clad width w, bonding zone (BZ), height h_B, heat affected zone (HAZ) as well as the wettability angles for the right side α_R and left side α_l, respectively (Fig. 1).
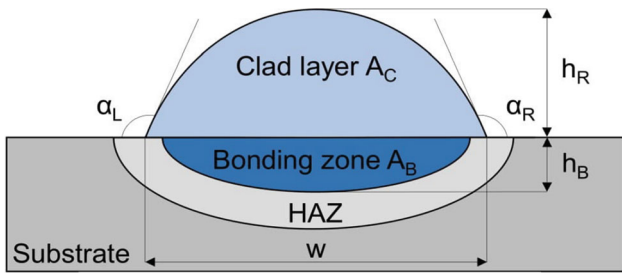
Table 1 Stellite™ 6 and EN-GJLP-200 chemical composition, wt.%

Coating	Co	Cr	W	C
Stellite™ 6 (Ref 22)	Bal.	27.9	4.7	1.3

	Ni	Fe	Si	Mn	Mo
	2.1	1.8	1.2	0.4	0.2

Substrate	Fe	C	Si	Mn	S
EN-GJLP-200 (Ref 23)	Bal.	3.3	2.4	0.3	0.1

Table 2 Process setup and parameters for coaxial laser cladding

Laser	v, mm/min	d_F, mm	d_L, mm	$\dot{V}_{SG}$, l/min
	800.0	20.0	5.0	8.0*

Nozzle	Type	α_N, °		
	Coaxial	90.0		

Powder	$\dot{m}_P$, g/min	$\dot{V}_{FG}$, l/min		
Feeder	25.0	1.5*		Ar*

*Gas argon

Fig. 1 Schematic geometrical measurement for a single-bead as cross section polish

2.3.4 Dilution. Dilution of single-beads η_B [%] was measured by area ratio between bonded substrate A_B and coating A_C total area based on cross sections (Fig. 1) (Ref 10):

$$\eta_A = \frac{A_B}{A_C + A_B} \cdot 100\% \tag{Eq 1}$$

According to Toyserkani, the dilution for coatings η_T [%] is determined based on the content of substrate material (here: Fe) in the deposited material Stellite™ 6 (Ref 8):

$$\eta_T = \frac{\rho_A(X_{A+S} - X_A)}{\rho_S(X_S - X_{A+S}) + \rho_A(X_{A+S} - X_S)} \cdot 100\% \tag{Eq 2}$$

where ρ_A [kg/m^3] is the density of the deposited material, ρ_S [kg/m^3] is the density of the substrate material, X_{A+S} is the percentage by weight of element X in the welding bead, X_S is the percentage by weight of element X in the substrate material and X_A is the percentage by weight of element X in the additive material. The SEM–EDS method was used to determine the Fe content quantitatively in the welding bead center on an area of 0.25 mm^2.

2.3.5 Scanning Electron Microscope—Energy Dispersive Spectrometer. The scanning electron microscope (SEM) Leo 1430 (co. Carl Zeiss AG) was used for imaging with a secondary electron (SE) and backscattered electron (BSE) detector at acceleration voltages of 15 to 20 kV. Coupled with an energy dispersive spectrometer (EDS) of type XFlash 6I30 (co. Bruker Corporation), the SEM–EDS method was used for space-resolved element distribution. For the quantitative microstructure analysis of the Stellite™ 6 welding beads, 8-bit grey value SEM images with BSE detector of cross sections were segmented and binarized. Through the image processing software Image J®, consequently, the following components and geometric parameters were examined in a reproducible manner:

- area fraction of Co solid solution (Co-SS), inter-dendritic eutectic (IE), carbides and pores,
- secondary dendrite arm spacing (SDAS), and lamella spacing (LS) of the interdendritic eutectic.

The determined volume fractions and geometric distances correspond to the arithmetic mean of two individual image analyses and 50 individual measurements for the respective laser power.

2.3.6 Electron Backscatter Diffraction. For the electron backscatter diffraction (EBSD) method, the detector e-Flash (co. Bruker Corporation) was used (Table 3).

The computer-assisted grain size investigation was carried out with the software Esprit 2.1 (co. Bruker Corporation), which generates ellipses for grains with the same area moments

Table 3 Setup for SEM coupled with an EBSD detector

SEM	Aperture, μm	Current, nA	
	50	1.7	
EBSD	Distance, mm	Angle, °	Exposure, ms
	16	70	80

Table 4 Setup for XRD measurements with $\theta - \theta$ goniometer

Tube	Detector	
X-ray lens	Parallel plate collimator, °	0.18
	β-Filter	Fe
	Soller slit, rad	0.02

Parameter	Single-beads	Multi-beads
Angular range, °		20.00-140.00
Step size, °		0.03
Step time, s	18	5
Divergence slit[a], °	1	10
Mask[a], mm	1	8

[a]Use on the tube side.

and calculates the arithmetic mean diameter (Ref 24). Moreover, the average grain size $\overline{D}$ [μm] was calculated using the standard ASTM E112-12 (Ref 25):

$$\overline{D} = \frac{\sum_{x=1}^{n} a_x = (D_n \cdot f_n)}{100\%} \tag{Eq 3}$$

where D_n [μm] is the respective grain size and f_n [%] is the corresponding proportion to form the product a_x [μm·%].

2.3.7 X-ray Diffraction. The x-ray diffractometer EMPYREAN (co. Malvern Panalytical GmbH) with a cobalt anode (λ_{K_α} = 1.79028 Å) was used for the qualitative phase analysis at an acceleration voltage of 40 kV and a current of 40 mA (Table 4). The phase identification was carried out with the evaluation software HighScore Plus (v. 4.5) (co. Malvern Panalytical Ltd).

2.4 Mechanical Investigation

2.4.1 Brinell Microhardness. The hardness of EN-GJLP-200 was determined using the Brinell method and the ISO 6506 standard (Ref 26). A hardness testing machine of type Testor 930/250 (co. Instron Wolpert GmbH) was used, and the measurement was carried out on specimens polished to 9 μm under the test condition HBW 2.5/187.5/15. The specified hardness values correspond to the arithmetic mean of 10 measurements. For the comparability of the substrate hardness and deposition material, the determined Brinell hardness (HB) according to the standard ISO 18265 was converted into the Vickers hardness scale (Ref 27).

2.4.2 Vickers Microhardness. The microhardness of the Stellite™ 6 beads was carried out according to Vickers using the ISO 6507 standard (Ref 28). For the measurements, a

microhardness tester of type VMHT/30 (co. Leica GmbH) was used on specimens polished to 1 μm under the test condition HV 0.05/15. The hardness values correspond to the arithmetic mean of at least three individual measurements.

3. Results

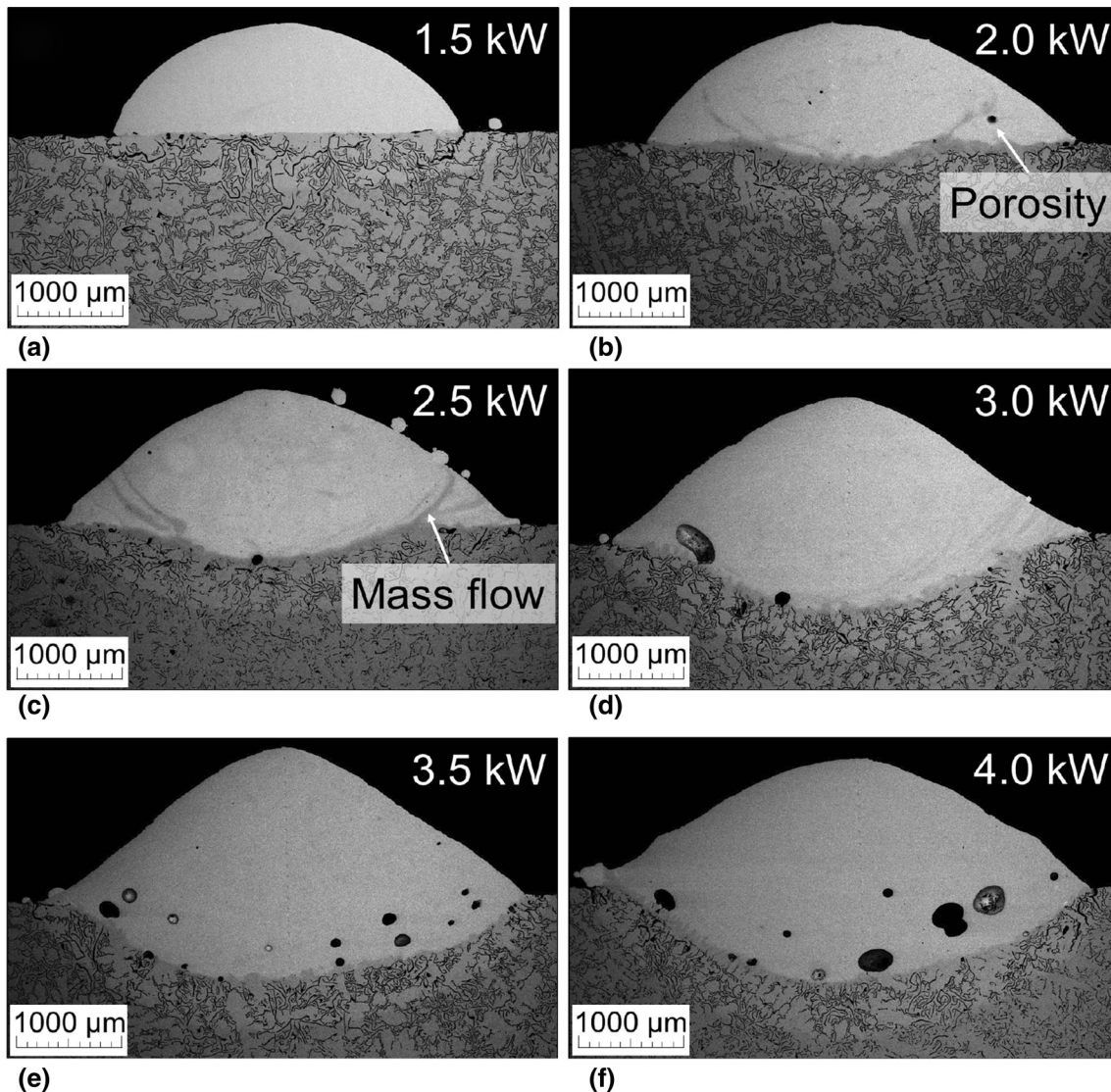### 3.1 Geometry of Single Beads

Figure 2 shows macro graphic images of single-bead cross sections. At a laser power of 1.5 kW, the deposited material is almost exclusively melted (Fig. 2a). Isolated agglomerate formation occurs on the surface of the weld beads. Within the welding beads with 2.0 to 2.5 kW the laser beam creates a deep and narrow penetration zone in the substrate and an isolated mass flow from the melt pool can be recognized (Fig. 2b and c). At 3.0 kW there is an increased arising of porosity in the interface area within single-beads (Fig. 2d, e and f).

The pores show characteristic features of gas inclusions with a smooth-walled and circular morphology. A formation of gas pores could be caused due to moisture content in the shielding/carrier gas and/or oxide layer because the substrate exhibited a thin layer of rust. In particular, the pores harm adhesion, ductility, and fatigue properties. Furthermore, the HAZ extends with increasing laser power, which is a direct indicator of the need for preheating and/or post-weld heat treatment to avoid excessive residual stresses and hence coating cracking (Ref 29).

Based on SEM images, the geometrical single-bead properties were evaluated under different laser powers, as shown in Fig. 3. The course of the wettability angle, width, and reinforced height corresponds to a logarithmic convergence and a performance of fit with a coefficient of determination close to 1, which can also be observed in studies of Ocelík et al. (Ref 30) and El Cheikh et al. (Ref 31).

The geometric relationship defined by Oliveira et al. between the width and reinforced height for single-beads: $\alpha = 180 - 2 \cdot \arctan(2 \cdot h_R/w)$ is also confirmed in the present series of experiments. An increase in laser power leads to a decrease in the reinforced height, which is a result of an increase in the bead width which also agrees with Oliveira´s investigations (Ref 32).

Fig. 2 Backscattered SEM micrographs of the cross-sectional area for (a), (b), (c), (d), (e), and (f) single-beads with the respective laser power
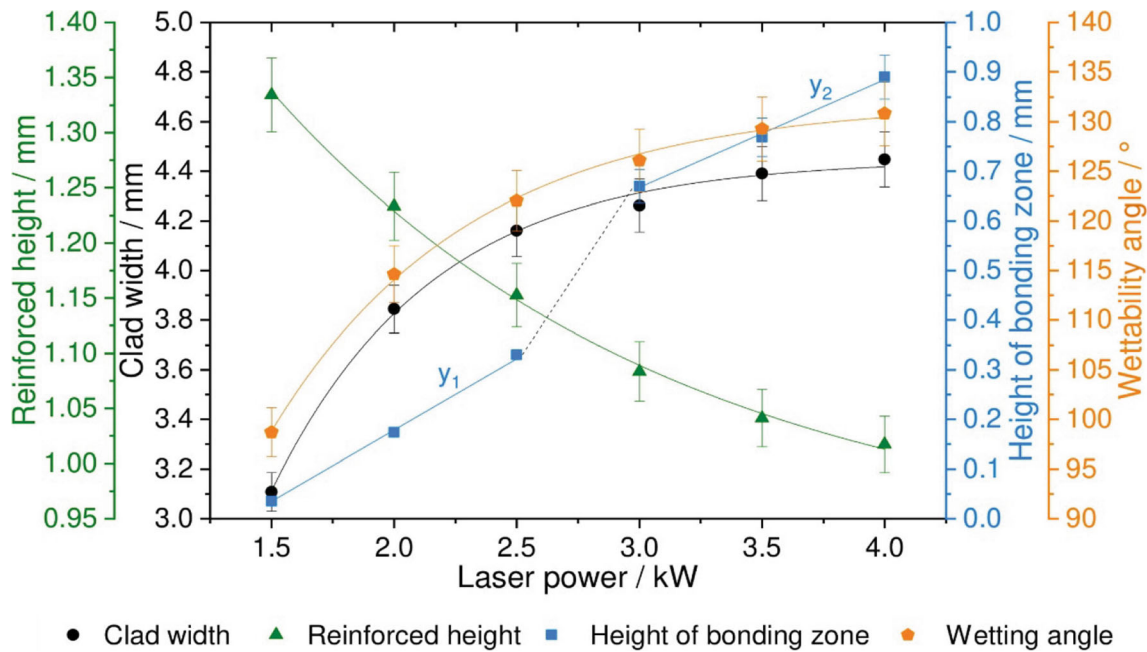
Fig. 3 Geometrical measurements of single-beads as a function of laser power. The specified wettability angle α corresponds to the average of α_R and α_L (Fig. 1)

The wettability angle is consistently greater than 90°, which reduces the occurrence of inter-run porosity and improves the coating quality (Fig. 6a and b) (Ref 30, 33-36).

The bonding zone has an abrupt rise between the laser powers of 2.5 and 3.0 kW. This represents a performance threshold and was also observed in previous investigations (Ref 7, 30, 32).

3.2 Dilution of Single- and Multi-Beads

Figure 4 illustrates the dilution and volume fraction of porosity obtained for (a) single-beads and (b) in comparison with multi-beads. The dilution increases with the laser power and shows a rising curve progression between the laser powers of 2.5 and 3.0 kW (Fig. 4a).

However, the small and close dilution observed for 1.5 and 2.0 kW indicates that both are inside the expected range for laser cladding being initially qualified for continuing examinations (Ref 37). Besides, the dilution does not vary significantly with the chosen Area- and Toyserkani-method.

A comparison between the dilution of single- and multi-beads—1.5 to 2.0 kW—confirmed the effectiveness of 30% overlap on reproducing the single-bead dilution to multi-beads (Fig. 4b). Overall, the dilution for multi-beads is lower compared to single-beads, which results in less influence on the substrate properties and is compliant with investigations of Paes et al. (Ref 22).

Without exception, the porosity increases steadily with the laser power, whereby the multi-beads have a higher volume fraction of porosity compared to single-beads (Fig. 4a and b).

3.3 Microstructure of the Weld Zones

An overview of the welding zones and microstructures within single-beads is shown in Fig. 5. The single-beads have a structure that is composed of the unaffected substrate material

EN-GJLP-200, a HAZ, a BZ, an interface, and as well as the deposition material Stellite™ 6 (Fig. 5a and b). The unaffected substrate has a pearlitic structure and the flake graphite has its original shape (Fig. 5c).

The BZ and HAZ expand toward the substrate with increasing laser power. On part of the substrate, structures of upper bainite and plate martensite are formed with a needle-shaped morphology in the interface (Fig. 5c and d).

On closer examination, upper bainite within a welding bead spreads further from the center toward the edges with increasing laser power (Fig. 5c). In addition, the hypoeutectic alloy Stellite™ 6 solidifies dendritically (Fig. 5d). These observations agree with studies by Luo et al. (Ref 6) and Atamert et al. (Ref 2).

Figure 6 shows the weld zones and microstructures in the interface and overlap zone (OZ) for multi-beads. Compared to single-beads, the multi-beads have similar compositions of weld zones and solidification structures (Fig. 6a and b). From the weld bead center, the height of the HAZ and BZ decreases toward the outside, which is lowest below the OZ. Bainite and martensite are also present in the interface, whereby the formation of bainite is more pronounced with increasing laser power on part of the substrate (Fig. 6c and d).

In the bead center, dendrites with a columnar shape grow vertically from the interface to the surface (I) and dendrites of a subsequent weld bead in, turn grow, orthogonally to the surface of a previous weld bead (II) (Fig. 6e and f). The structure in the OZ is coarser compared to its surrounding. These findings can also be observed in studies by Lin et al. (Ref 38).

3.4 Microstructure of Stellite™ 6

The microstructure of Stellite™ 6 is comprised of a hypo-eutectic dendritic matrix, which is a β-Co solid solution with a metastable fcc lattice and an interdendritic lamellar eutectic, which consists of predominant β-Co as well as Cr rich and
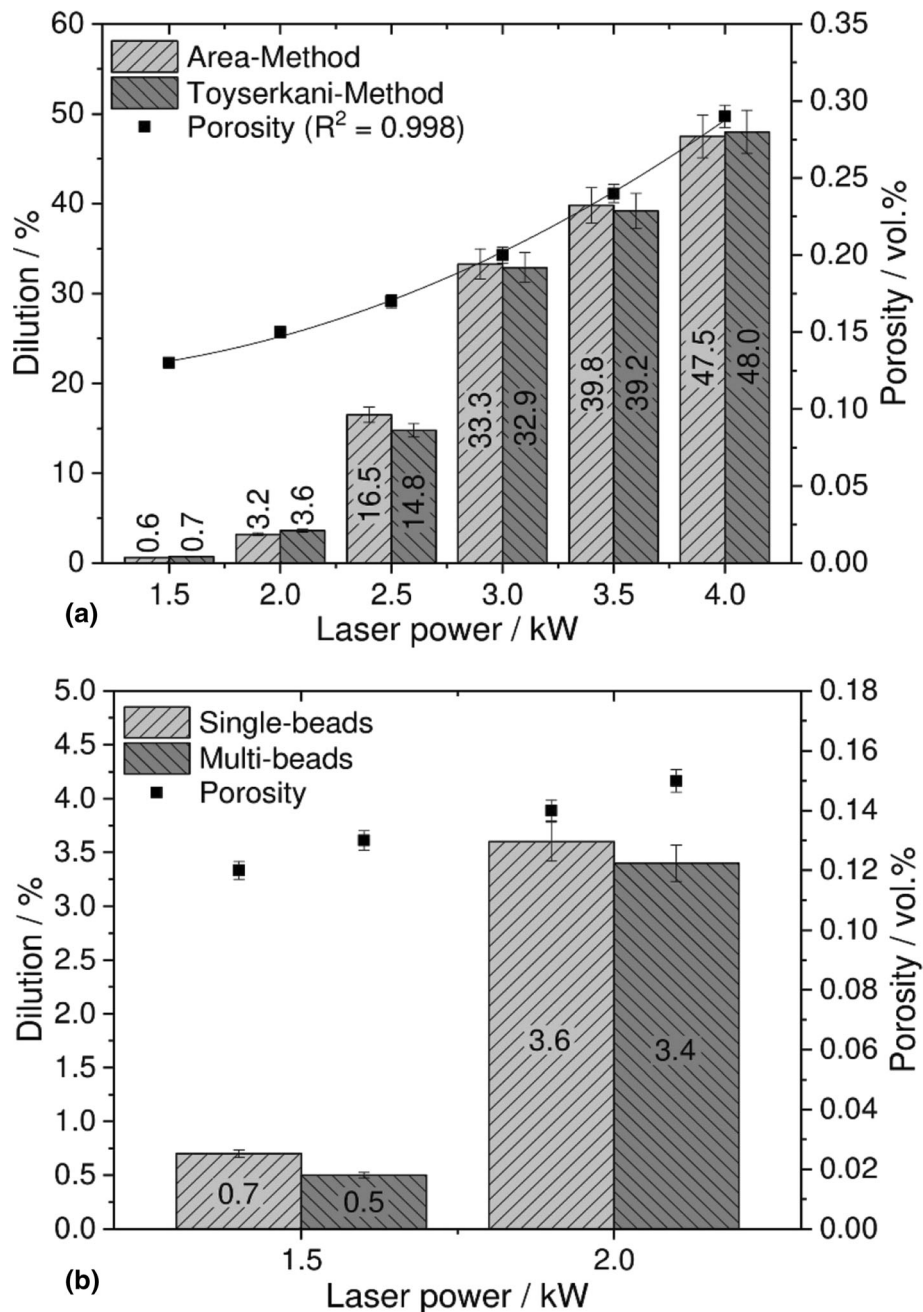
Fig. 4 Dilution measured with Area- (Eq 1) and Toyserkani-method (Eq 2) as well as the volume fraction of porosity as a function of the laser power for (a) single-beads and (b) single-beads in comparison with multi-beads

blocky W carbides with a homogenous distribution (Fig. 7). On closer inspection, a lozenge shape pattern can be seen within the matrix for all laser powers that was also observed in further studies (Ref 39-41). This pattern is caused by the low stacking fault energy (SFE) (γ_{fcc-Co} = 10-50 mJ/m^2 (Ref 42)) and residual stresses within the deposits during cooling (Ref 2, 43). These induce the formation of stacking faults on {111} planes (Ref 41, 44).

The area-resolved distribution of the main alloy elements in the microstructure is given in Fig. 8. The dendritic metal matrix

is rich in Co and the interdendritic eutectic has an increased Cr content. These findings about the microstructure and EDS mapping are consistent with Luo et al. (Ref 6) and Houdkova et al. (Ref 4).

3.5 Qualitative Phase Analysis

The diffractograms of (a) single-beads and (b) in comparison with multi-beads are plotted for the respective laser power in Fig. 9 to analyze the diffractogram patterns of the cross-
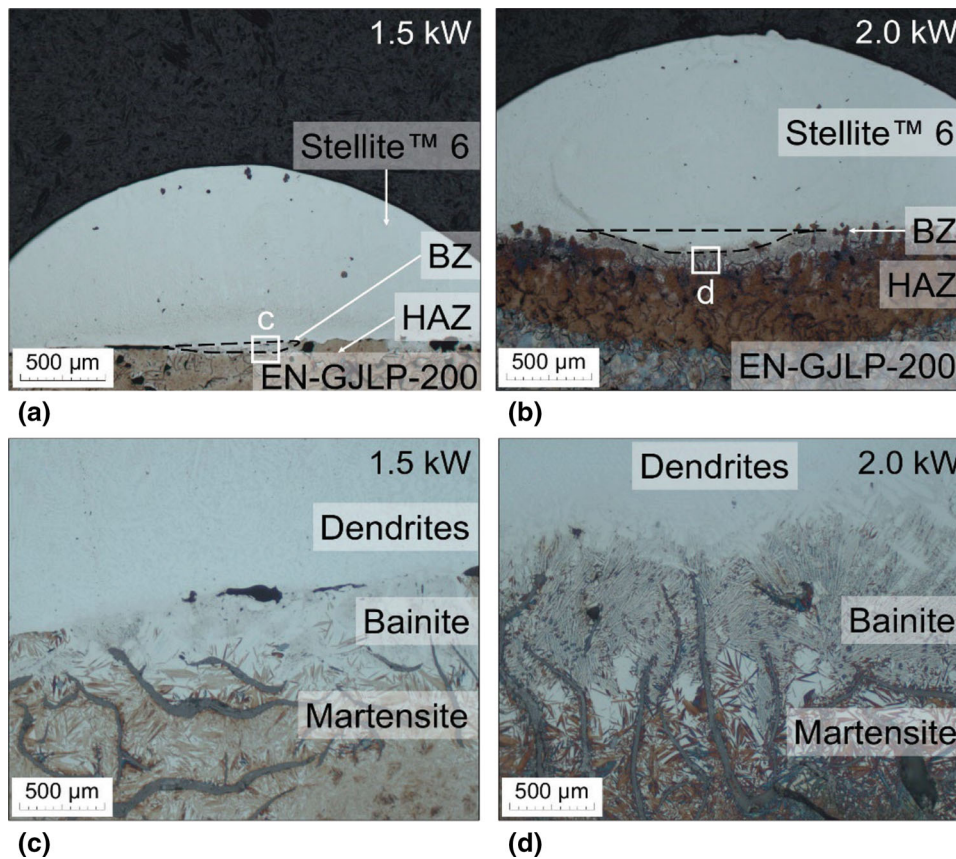
Fig. 5 Optical microscope images of the (a), (b) welding zones and (c), (d) interfaces based on cross sections of single-beads with 1.5 and 2.0 kW laser power

sectional phases within the coating system. On the substrate side, the phases α-Fe and Fe_3C of the pearlitic structure in combination with the graphite of the lamellae can be seen (Fig. 9a and b). Furthermore, a martensitic structure, the mixed crystal Fe_2Si, and carbide $Fe_4C_{0.63}$ have formed. The examined angle range for single-beads is without exception a β-Co metal matrix existent (Fig. 9a). The main hard phases are the metastable Cr carbide Cr_7C_3 and W carbide W_2C. In addition, the mixed crystal $FeCr_3$ was created. These determined phases for single-beads are consistent with previous studies (Ref 4, 10, 22, 45-47). However, higher laser power or heat input induces smaller peaks of the carbide Cr_7C_3. Besides, there is an enlargement of the peak (50 to 53°), which probably results from the presence of stacking faults (Ref 48). In comparison with single-beads, the metal matrix of multi-beads still consists of α- and β-Co solid solution (Fig. 9b), which was also proven in the research of Houdková et al. (Ref 4). The hard phase $Cr_{23}C_6$ and mixed crystal Co_3W are present, too.

3.6 Quantitative Microstructural Analysis

In Fig. 10 the volume contents of the individual microstructural components for single- and multi-beads are characterized quantitatively depending on the laser power. The volume content of the metal matrix (β-Co solid solution) increases in the single-beads concurrent with the laser power (i.e., heat input

or dilution), whereas the volume content of the interdendritic eutectic and the carbides decrease.

Parallel, the curves have an escalating progression between the laser powers 2.5 and 3.0 kW. Overall, this trend also agrees with studies by Paes et al. (Ref 22). Investigations with comparable process parameters to the single-bead at 1.5 kW laser power have shown a similar phase composition (Ref 47, 49-52). The value patterns of the coatings have a similar tendency compared with the single-beads, but they are less pronounced.

Figure 11 shows (a) the secondary dendritic arm spacing λ_1 and (b) interdendritic lamellar spacing λ_2 for single-and multi-beads as a function of the laser power. Both parameters of single-beads increase linearly with the laser power (Fig. 11a and b). For instance, Frenk et al. researches in laser cladding of Stellite™ 6 with comparable process parameters showed that the local solidification times are in the range of 1-2 ms and local cooling rates between 300 and 400 K/s to produce a SDAS of 2-3 μm like in the present work (Ref 16). Paes and Scheid deposited Stellite™ 6 by plasma transferred arc (PTA) and examined an SDAS between 10 and 15 μm. Furthermore, in comparison with the results of the dilution (Fig. 3) and quantitative microstructural analysis (Fig. 10), a performance threshold between the laser powers of 2.5 and 3.0 kW does not occur. The value ranges of SDAS and LS are compliant with a
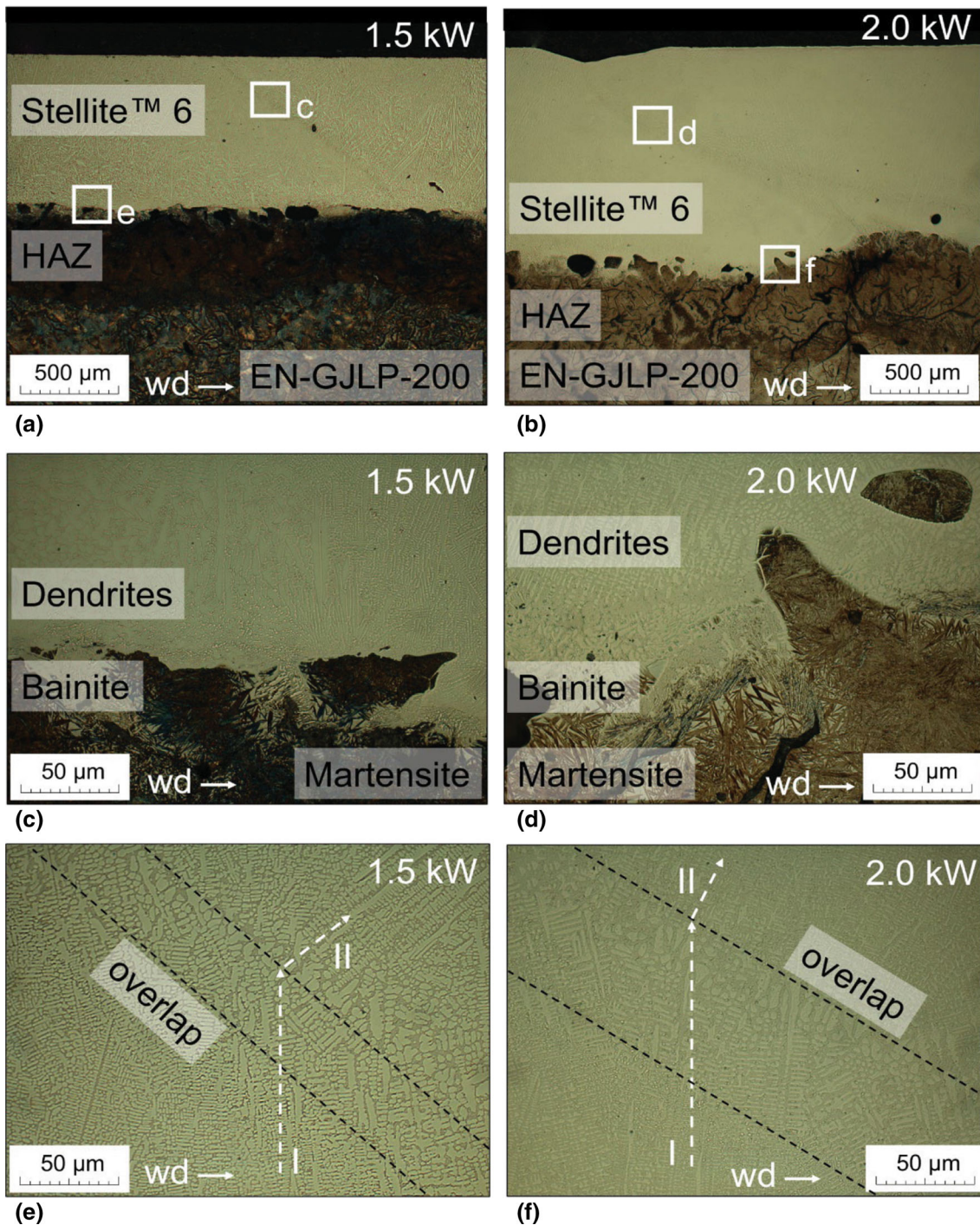
Fig. 6 Optical microscope images of the (a), (b) welding zones, (c), (d) interfaces and (e), (f) overlap zones based on cross sections of multi-beads with 1.5 and 2.0 kW laser power. Multi-beads with 1.5 kW laser power are ground flat. wd = welding direction

couple of studies on laser cladding with Stellite™ 6 (Ref 16, 49, 51, 53). The SDAS and LS of the coatings have a similar tendency to the single-beads, whereby the values are increased by an average of 3%.

3.7 Microhardness of Single-Beads

Figure 12 illustrates the hardness profiles of single-beads with 1.5 to 4.0 kW laser power, which can be divided into four sections. Up to about 250 μm, there is the respective hardness maximum of Stellite™ 6. In the further course, the hardness

steadily decreases toward the interface. In the HAZ, there is an escalating increase in the hardness present. With increasing laser power, the HAZ shifts to longer distances due to a performance threshold, which occurs abruptly between Mode I and Mode II.

Subsequently, the hardness of the unaffected substrate material is present. These determined hardness profiles are comparable with studies on laser cladding (Ref 49, 52-55) and also plasma transferred arc welding (Ref 10, 49) of Stellite™ 6.
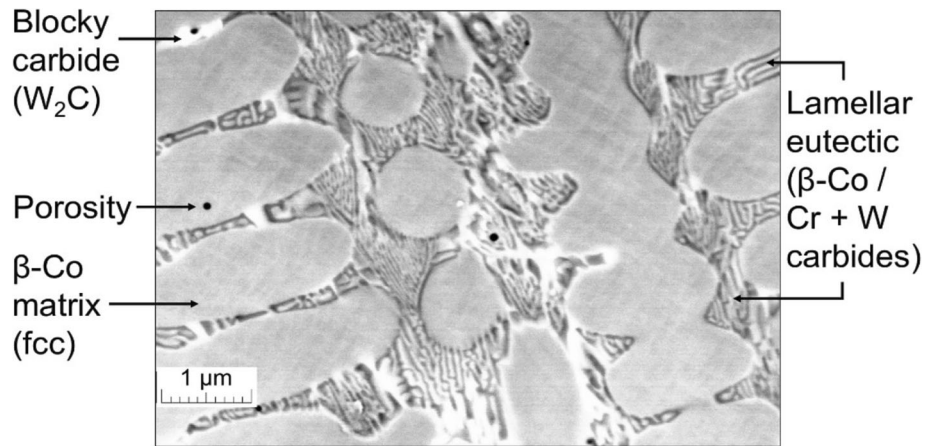
Fig. 7 BSE-contrast of the Stellite™ 6 microstructure in the center based on cross section of a single-bead with 1.5 kW laser power
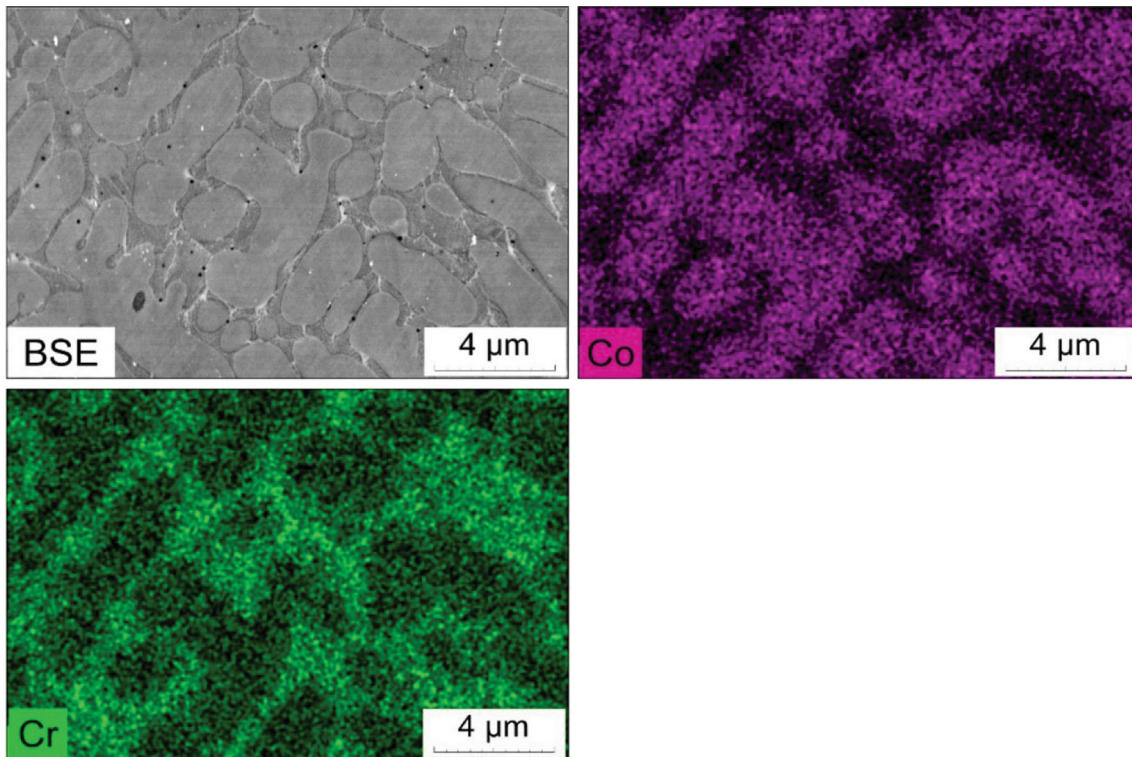

Fig. 8 SEM–EDS mapping of the Stellite™ 6 microstructure in the center based on cross section of a single-bead with 1.5 kW laser power

The EDS concentration profile for a single-bead with 1.5 kW laser power shows a homogeneous distribution of the main alloying elements in the Stellite™ 6 coating and substrate material with a narrow interface area (Fig. 13). Though, the present concentration profile is representative of the other laser powers for single-beads, whereby a similar course was observed. This suggests, that the hardness profiles are primarily influenced by a microstructural change within the deposition material and substrate, which is also described in studies by van Mol Otterloo et al. (Ref 19) and Zhong et al. (Ref 20).

3.8 Microhardness of Multi-beads

In Fig. 14, the hardness profiles of the Stellite™ 6 multi-beads in the transverse direction are shown. Within the first two weld beads, the hardness of the respective coating increases to a nearly constant level with small deviations around the arithmetic mean value until the last weld bead is reached. The hardness of multi-beads with 1.5 kW laser power is increased by 6%. Moreover, the multi-beads show a similar average value of hardness with 565 and 532 $HV_{0.05}$ for 1.5 and 2.0 kW
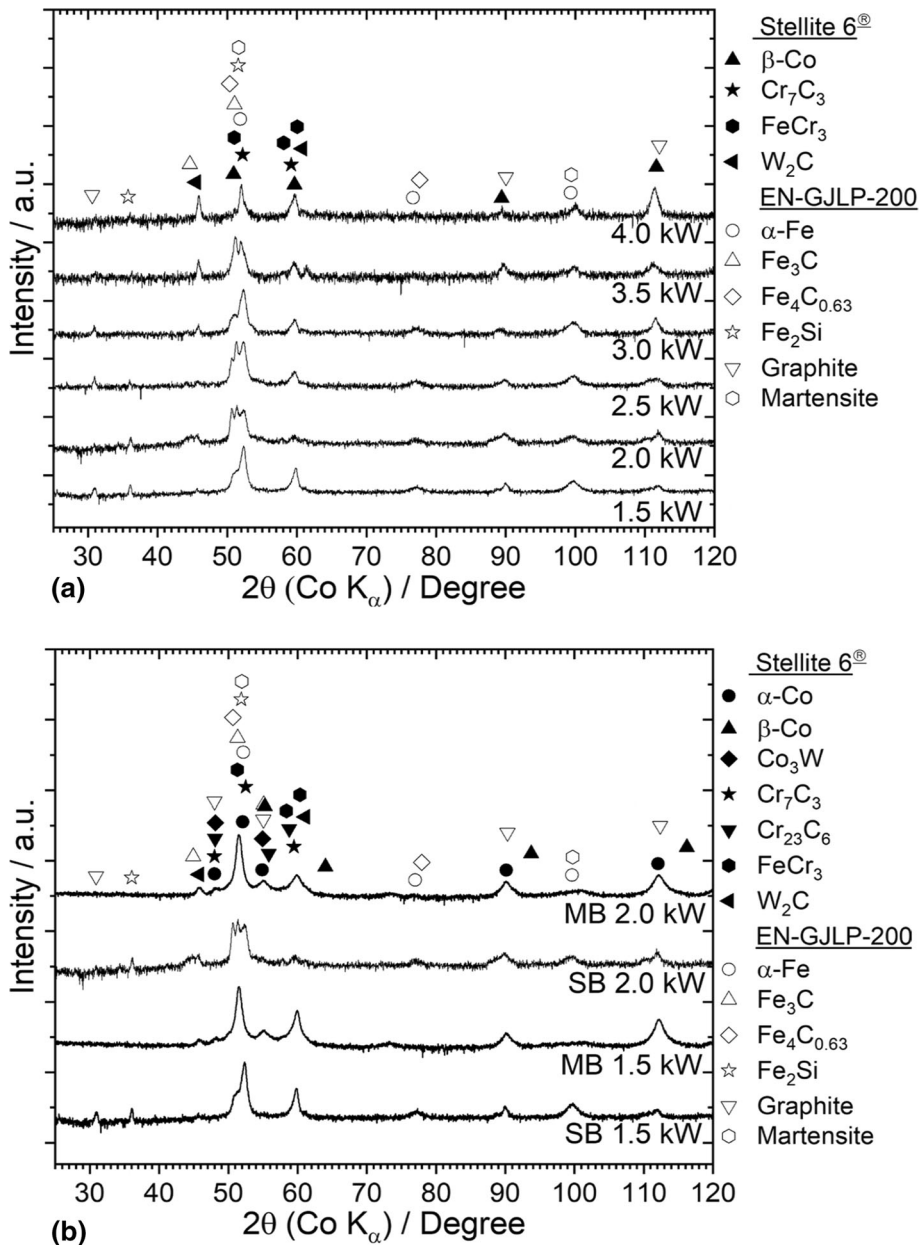
Fig. 9 XRD patterns as a function of the laser power for (a) single-beads and (b) single-beads in comparison with multi-beads based on cross section polishes. Solid markings are phases in Stellite™ 6 and blank markings are phases in grey cast iron

compared to single-beads processed with the same laser power and distance to the surface. This course of hardness profiles is confirmed in studies by Luo et al. (Ref 6) (used laser cladding) and Paes et al. (Ref 22) (used plasma transferred arc). Across the coating, there was a non-uniform hardness profile under alternating fluctuations, which was already observed by D´Oliveiraa et al. (Ref 53).

3.9 Grain Structure Analysis

The phase composition and grain size distribution of single- and multi-beads determined by using EBSD are graphically compared in Fig. 16. Without exception, β-Co is present in the coatings (Fig. 15a, b, e, and f).

Furthermore, there is a fine-grained seam with an undirected dendritic structure near the surface (Fig. 15c, d, g, and h), which was also detected by Farnia et al. (Ref 56). In the center of single-beads, numerous fine columnar grains grow uniformly and perpendicularly from the interface to the surface. As the laser power decreases, the crystallographic preferential direction of the columnar grains becomes more homogeneous (Fig. 15c and d). The expansion rate of the grains is more pronounced in the single-bead center compared to the surface areas (Fig. 15d). These described tendencies can also be seen within the multi-beads (Fig. 15e-h).
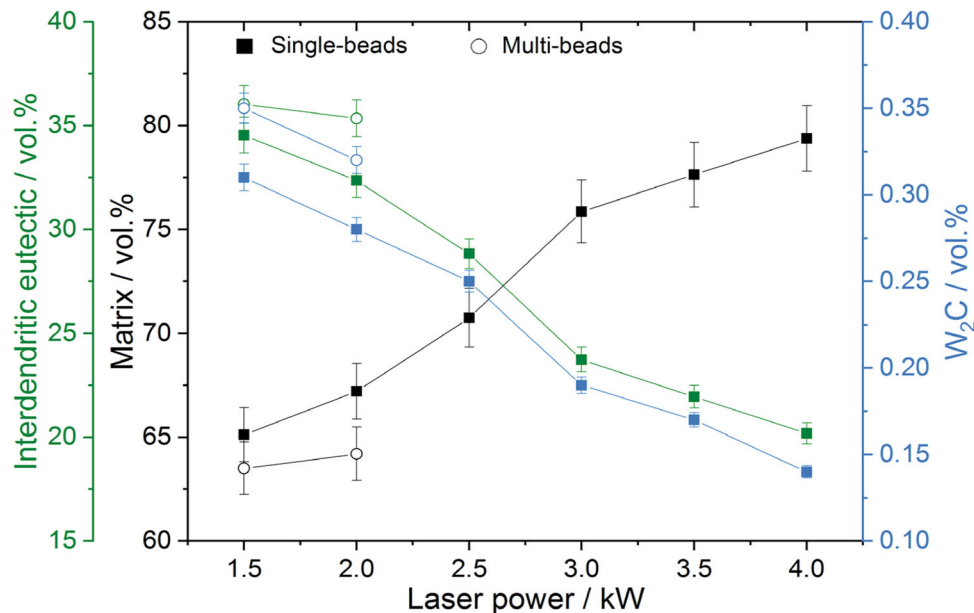
Fig. 10 Quantitative phase analysis by means of BSE images using ImageJ® to identify the volume content for the metal matrix, interdendritic eutectic and hard phase (M_6C) as a function of the laser power based on cross section polishes

3.9.1 Grain Size Distribution. Figure 16 shows the grain size distribution histogram for multi-beads. With increasing laser power, the grain size distribution broadens, and the averages shift to larger values. The EGS (Eq 3) calculation for the applied coatings results in 52.6 μm^2 for 1.5 kW and 76.1 μm^2 for 2.0 kW laser power. The results for quantifying the grain size are thus consistent with the findings from Fig. 15.

4. Discussion

4.1 Bead Geometry and Dilution

An increasing laser power induces an intensified melting of the substrate and causes more pronounced melt dynamics/dilution and temperature rise (Ref 29, 57). As a result, the surface tension of the weld pool decreases (Ref 31), and the wettability angle converges asymptotically: $\cos(\alpha) \rightarrow 1$, whereas the height decreases in parallel with a constant powder feeding rate (Ref 8). The Fe melt has a positive surface tension gradient with a maximum in the weld pool center and a minimum toward the edges (Ref 58, 59). This effects a convergent Marangoni flow within the melt as a dominant convection mechanism for uniform mixing of the present elements in the entire volume of a weld bead/coating and creates a deep and narrow BZ (Ref 7, 29).

According to Jouvard et al., the sudden increase in height in the bonding zone between the laser powers of 2.5 and 3.0 kW is due to a power threshold being exceeded. In this case, there is more radiation energy than is necessary for the complete melting of the Stellite™ 6 powder particles, whereby the excess radiant energy causes an increased melting of the substrate (Ref 60). The concentration gradient is another driving force for mass transfer/diffusion, but due to the high cooling rate

($>10^2$ K/s) during the laser cladding, the time interval is limited to a few seconds and therefore subordinate (Ref 22, 29).

In the process, molten pool spreading, or enlargement is a result of the laser Gaussian energy distribution as the laser power increases (Ref 61), and the bead width tends to reach the nominal laser spot size of 5 mm. The reduced dilution of multi-beads to single-beads depends primarily on the laser power and secondarily on the degree of overlap. The first weld bead of a coating exhibits a nearly identical dilution to a single weld bead (Ref 22). The second weld bead has a reduced dilution since the substrate and previous weld bead are molten according to the overlap, which subsequently affects an entire coating (Ref 30). Research by Houdková et al. showed, that laser clad coatings, containing lower amounts of Fe due to the dilution with the substrate, exhibit a more pronounced wear resistance (Ref 4).

4.2 Microstructure

The microstructural properties of the substrate and Stellite™ 6 coatings depend directly on the alloy composition, dilution, and present temperature profile during the laser cladding (Ref 4). From the substrate analysis close to the welding interface—after heating and rapid cooling associated with laser cladding thermal cycling—the bonding zone showed high-carbon martensite since the substrate has 3.3 wt.% average carbon.

The formation of martensite is based on a diffusionless and cooperative shear movement of atomic groups when the austenite form a tetragonal lattice distortion (Ref 59). In addition to martensite, upper bainite is also formed most frequently at the bead center, in which a higher laser power seems to spread its formation to the edges. This effect correlates with the Gaussian distribution and a decrease in the cooling rate with increasing laser power (Ref 61, 62). It should be noted that the formation of martensite is linked to internal stresses, which
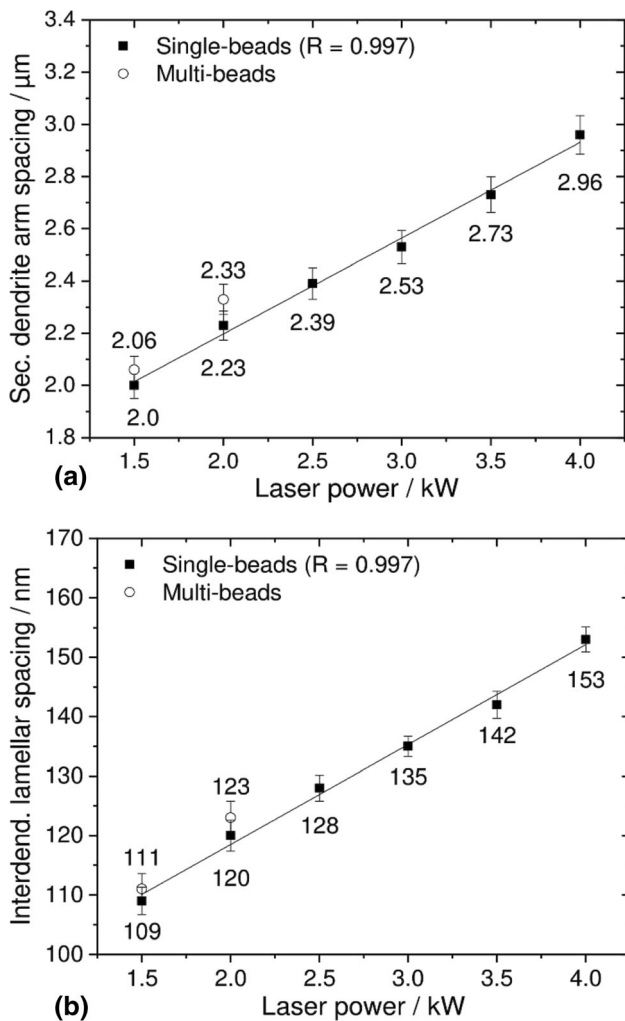
Fig. 11 Evolution of the (a) secondary dendritic arm spacing λ_1 and (b) inter-dendritic lamella spacing λ_2 for single- and multi-beads as a function of the laser power based on cross-section polishes

detrimentally influence tensile and fatigue strength as well as corrosion resistance (Ref 2).

Besides, the structure of the Stellite™ 6 alloy is based on Frenk´s state diagram (Ref 16). In the binary system of β-Co and M_7C_3, the solidification of the hypoeutectic melt occurs primarily due to thermal conduction from the weld pool to the substrate material since the thermal conductivity coefficient of Fe (λ_{Fe} = 50.00 W/mK) and Co (λ_{Co} = 14.82 W/mK) is significantly higher compared to the protective gas atmosphere of argon (λ_{Ag} = 0.018 W/mK) (Ref 59). Thus, the substrate acts as a heat sink, whereby the highest crystallization velocity is present in the interface because the temperature gradient is low (Ref 33). However, the metal matrix of the coatings consists of α- and β-Co solid solution in comparison to single-beads. In this connection, the cooling rate decreases holistically within coatings, since more heat energy is introduced into the component overall (Ref 11, 63). At the same time, there is partial remelting in the overlapping zones (Ref 4). These conditions favor the local formation of the thermodynamically

more stable α-Co with a hexagonal closest packed (hcp) crystal lattice (Ref 4, 64).

The primary metal matrix grows as dendrites from the interface toward the solidification isotherms due to the highly directed heat dissipation into the substrate (Ref 65). The overall high cooling rate during laser cladding increases the temperature gradient and reduces the crystallization rate, inducing the growth of columnar dendrites (Ref 59). In the upper part of the welding beads, there are equiaxed dendrites (Ref 65) since the uniform heat dissipation in three directions prevents a preferred direction of growth (Ref 32). Thereby, the equiaxed dendrites continue to shrink with increasing distance from the welding bead center, since the Gaussian distribution of the laser power decreases toward the laser beam diameter, which further accelerates the cooling (Ref 62).

The grain size or the number of primary dendrites formed from a melt pool depends on the size of crystal nuclei (Ref 66). They must have exceeded a critical nucleus radius, which increases with the temperature (Ref 67). So, a decreasing laser power raises the number of available nuclei for the crystallization and decreases the crystallization velocity. Consequently, welding beads with 1.5 kW show a more fine-grained primary structure, which in turn shows a more homogeneous crystallographic orientation and growth direction along the solidification isotherms (Ref 59).

The dendrites consist of a Co-Cr-W solid solution, which also contains Fe with increasing dilution because the high cooling rate of laser cladding generates the metastable β-Co and γ-Fe with a fcc crystal lattice. Besides, they are 100% soluble in each other due to a difference in atomic radii (Ref 63). Therefore, the volume fraction of the primary matrix or solid solution increases compared to the inter-dendritic eutectic and hard phases with increasing laser power (Ref 9, 21, 48), which improves the ductility and adhesion of the coatings (Ref 68). On the other hand, Luo et al. have verified that the wear resistance of Stellite™ 6 coatings decreases with the reduction of M_7C_3 and W_2C carbides at the interdendritic regions (Ref 6).

The SDAS increases linearly in parallel with the laser power because the crucial process parameter in secondary dendrite coarsening is the heat input, which in turn alters the temperature gradient solid–liquid and, thus, the crystallization velocity (Ref 15, 52, 67). This leads to maturation processes in which the small secondary arms dissolve in favor of the larger ones with increasing laser power (Ref 66). The coarse dendritic structure in the overlap zone of Stellite™ 6 coatings is at the beginning of a new bead solidification because the previous bead acts as a heated substrate and reduces the cooling rate respectively increases the crystallization velocity (Ref 3, 5). With further cooling, the eutectic residual melt solidifies and surrounds the dendrites with a lamellar eutectic consisting of β-Co solid solution and hard phases (Ref 15, 68), whereby Co, Cr, and W are the metallic base, respectively (Ref 51). Besides, the thermodynamically more stable Cr carbide $Cr_{23}C_6$ can form within the coatings starting from the metastable Cr_7C_3 (Ref 69, 70), since there is a lower cooling rate compared to single-beads (Ref 10, 62). The temperature gradient or solidification cooling rate is decisive for the eutectic lamellar growing kinetics, dictating its lamella spacing. The increase in laser power affects an increasing melting temperature, which results
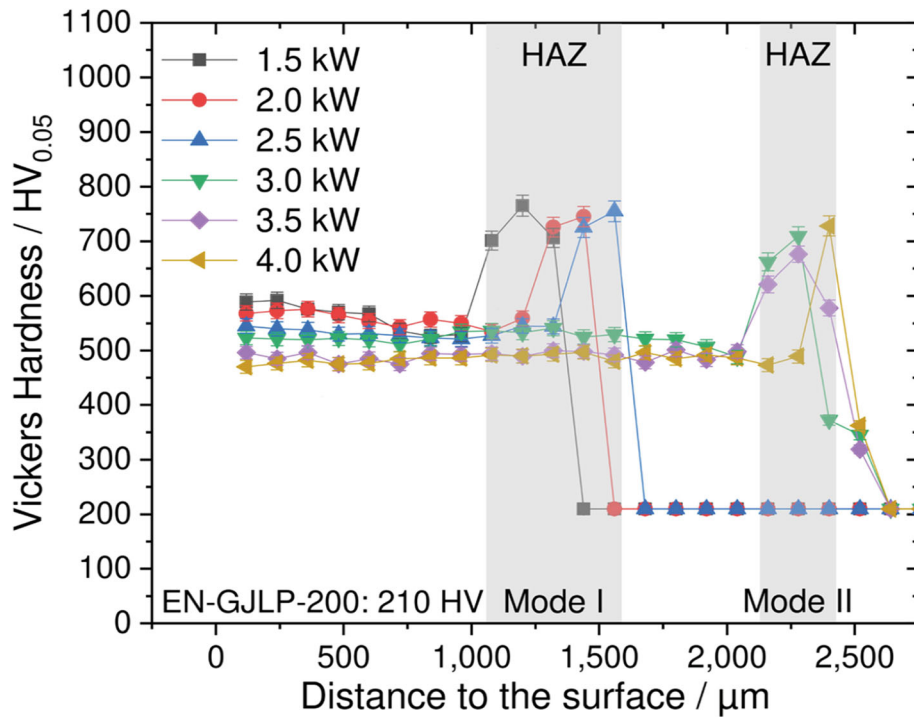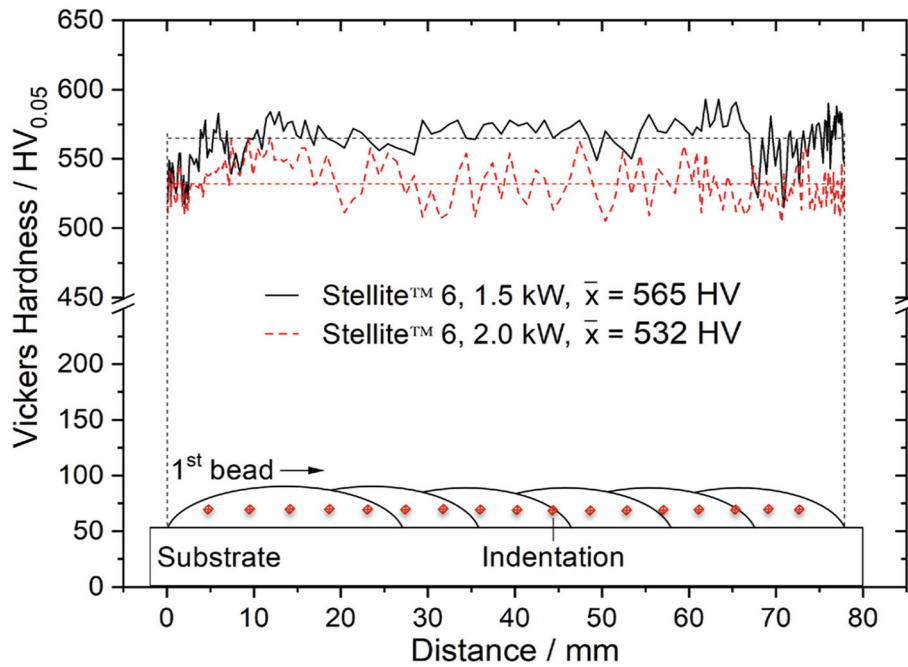
Fig. 12 Hardness profiles of single-beads with 1.5 to 4.0 kW laser power depending on the distance to the surface based on cross section polishes
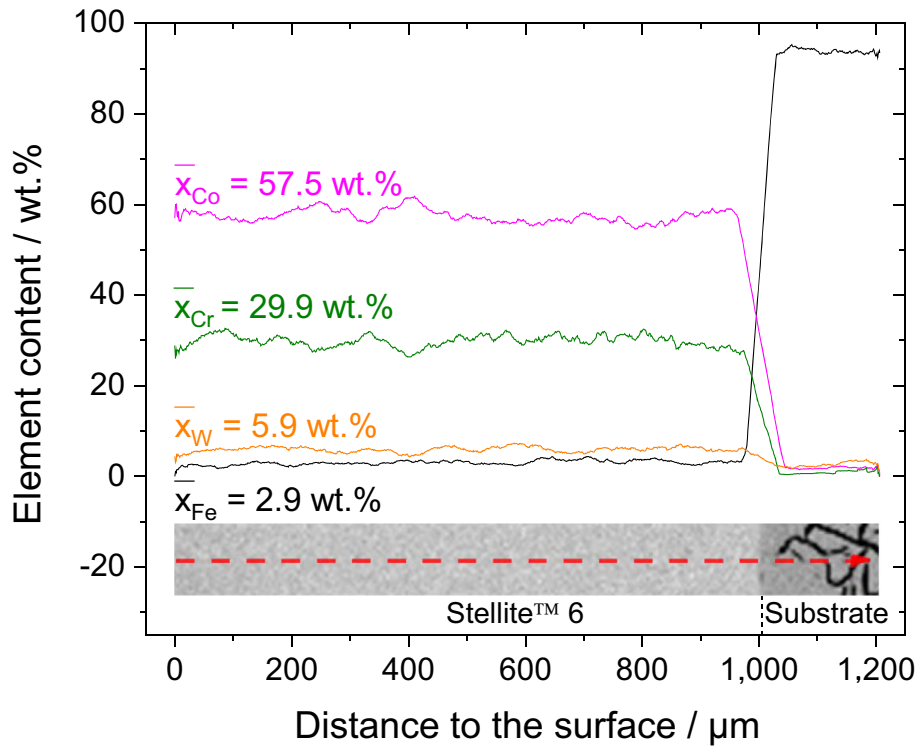
Fig. 13 EDS concentration profile for a single-bead with 1.5 kW laser power based on cross-sectional area, which is supportive visualized by a BSE image

Fig. 14 Hardness profiles of multi-beads for the laser powers 1.5 and 2.0 kW in transversal alignment with a schematic mapping of the measurement history. The distance between the indentations across the multi-beads is variable for the detection of possible hardening effects. The vertical distance between the measurement series and the surface is 0.5 mm

in a reduction of available nuclei. Accordingly, the number of lamellae decreases which ultimately increases the lamella spacing (Ref 66).

4.3 Microhardness

The four sections of the hardness profiles correlate with the characteristic sections of a weld bead (Fig. 12). The respective hardness maximum of single-beads is close to the surface because there is a fine-grained edge of equiaxed dendrites/grains (Fig. 15). In the further course, the hardness decreases toward the interface. This effect is linked with an increasing Fe content to the interface according to different investigations, which raises the SFE and stabilizes the β-Co matrix (Ref 1, 3, 6, 44, 67). The SFE of Stellite™ 6 (γ_{fcc-Co}= 10-50 mJ/m^2) is low compared to Fe ($\gamma_{Fe} = 140 \pm 40$ mJ/m^2) (Ref 41), whereby the dislocations tend to have a planar sliding character (Ref 6). Consequently, Fe reduces the critical stress for the transverse sliding of dislocations and caused a softening (Ref 67), in which the ductility and the tendency to adhesion are more pronounced (Ref 68). However, in the present EDS concentration profiles determined for single-beads, there is without exception a constant Fe content between the surface and welding interface (Fig. 13). Thus, the influence of Fe on the hardness profiles is subordinate in the present study. Besides the obvious reduction in the solid solution hardening elements (Cr and W) due to the increased and homogenous dilution of Fe, there were adopted two additional mechanisms accounted for the hardness reduction of single-beads. Accordingly, the SDAS and grain size are also presumably responsible for a hardness reduction toward the welding interface because they increase in parallel with the laser power (Ref 19, 37, 48,

56). The steep increase in hardness in the bonding zone can be attributed to the formation of plate martensite (Ref 71).

The displacement of the bonding zone to higher distances from the surface is exceeding the power threshold from a laser power of 3.0 kW, which causes a deeper penetration zone into the substrate. Further, the hardness of the bonding zone decreases with increasing laser power since a lower cooling rate affects the augmented formation of bainite along with the interface (Ref 5).

The hardness of the Stellite™ 6 coatings increases within the first two to three weld beads which is in correlation with a reduced dilution/Fe content due to the overlap (Ref 21). The non-uniform hardness profiles across the coatings are based on an alternating fine and coarse microstructure as well as the dilution (Ref 48, 52). Furthermore, in the weld bead center there is a coarser microstructure and more pronounced dilution in comparison to the overlap zones (Ref 20).

5. Conclusion

In this preliminary study, grey cast iron EN-GJLP-200 was coated with cobalt-base alloy Stellite™ 6 by using laser cladding to produce a cost-effective brake disk with enhanced wear and corrosion resistant as well as optical properties. Therefore, the effect of various laser powers was evaluated according to the bead geometry, dilution, microstructure, and hardness. The main conclusions can be summarized as follows:

- The geometric characteristics of a weld bead depend directly on the selected laser power and spot size. The
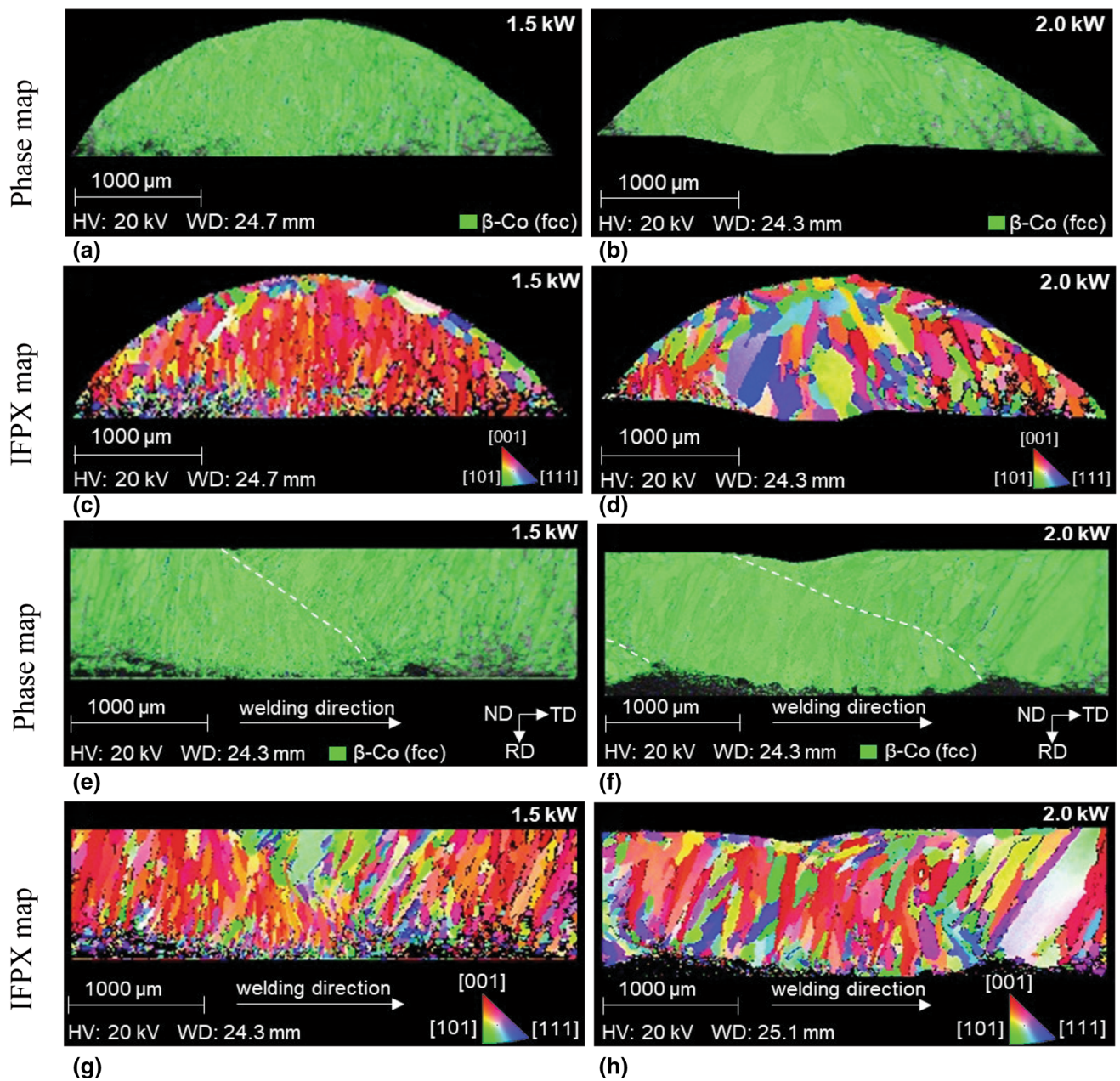
Fig. 15 EBSD images of (a), (b)/(e), (f) phase maps and (c), (d)/(g), (h) IFPX maps of cross sections for single- and multi-beads with 1.5 and 2.0 kW laser power. The coating with 1.5 kW laser power was ground flat before the measurement

bonding zone increases with the laser power while the height of a weld bead decreases. The wettability converges with $\cos(\alpha) \to 1$ and the width converges against the spot size.

- From the single-bead qualification, the porosity increases in parallel with higher laser powers (from 3.0 kW on), probably because of the substrate gas generation. Thus, laser powers of 1.5 and 2.0 kW with an overlapping ratio of 30% enabled the processing of coatings with an acceptable dilution ($< 5\%$) and porosity level (< 0.2 vol. %).

- The microstructure of the coatings consists of α- and β- Co rich, columnar dendrites as matrix and an inter-dendritic network, which contains eutectic lamellar Cr carbides (Cr_7C_3, $Cr_{23}C_6$) and blocky W carbide W_2C. From the SDAS and eutectic lamellar spacing, the finer and promising microstructures were obtained at 1.5 and 2.0 kW laser powers.

- The respective hardness maximum of the coatings was measured close to the surface, associated with a fine-grained edge revealed by EBSD. A non-uniform hardness profile across the coatings is based on alternating fine and coarse microstructural characteristics as well as the dilu-
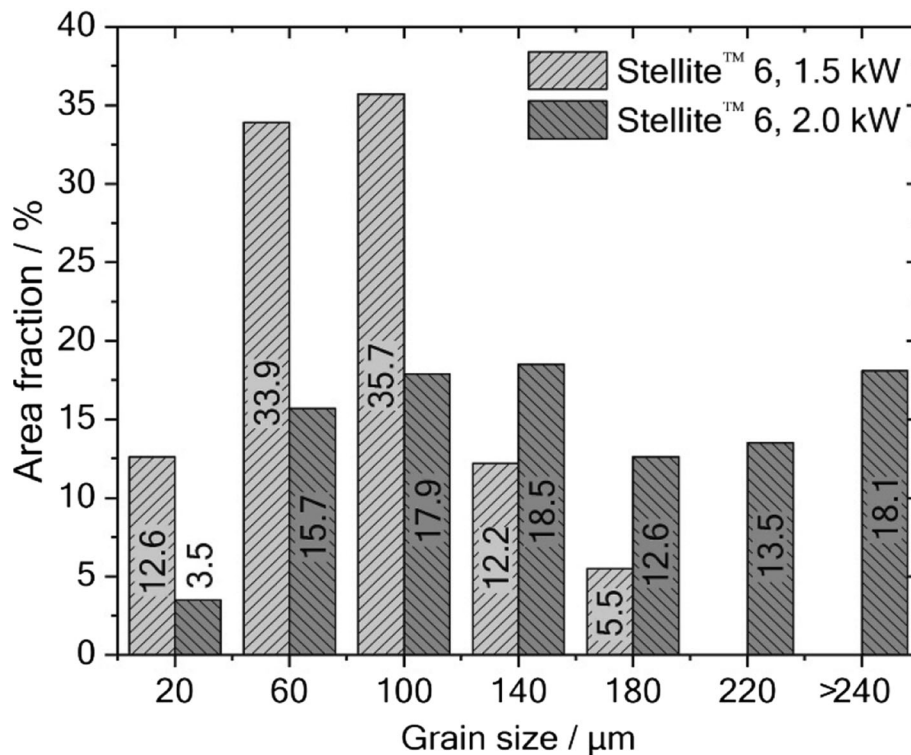
Fig. 16 Distribution of grain size based on EBSD measurements for multi-beads with 1.5 and 2.0 kW laser power based on cross section polishes

tion. Within the heat-affected zones, the formation of martensitic leads to an increase in hardness.

Conflict of interest

The author(s) declared no potential conflicts of interest concerning the research, authorship, and/or publication of this article.

Open Access

References

1. S. Apay and B. Gulenc, Wear Properties of AISI 1015 Steel Coated with Stellite 6 by Microlaser Welding, *Mater. Des.*, 2014, **55**, p 1–8. https://doi.org/10.1016/j.matdes.2013.09.056
2. S. Atamert and H. Bhadeshia, Comparison of the Microstructure and Abrasive Wear Properties of Stellite Hardfacing Alloys Deposited by Arc Welding and Laser Cladding, *Metall. Trans.*, 1989, **20**, p 1037–1054
3. P. Ganesh, A. Moitra, P. Tiwari, S. Sathyanarayanan, H. Kumar, S. Rai, R. Kaul, C. Paul, R. Prasad, and L. Kukreja, Fracture Behavior of Laser-Clad Joint of Stellite 21 on AISI 316L Stainless Steel, *Mater. Sci. Eng.*, 2010, **527**, p 3748–3756. https://doi.org/10.1016/j.msea.2010.03.017
4. Š Houdková, Z. Pala, E. Smazalová, M. Vostřák, and Z. Česánek, Microstructure and Sliding Wear Properties of HVOF Sprayed, Laser Remelted and Laser Clad Stellite 6 Coatings, *Surf. Coat. Technol.*, 2017, **318**, p 129–141. https://doi.org/10.1016/j.surfcoat.2016.09.012
5. Š. Houdková, O. Soukup, M. Prantnerová, Z. Pala, Comparison of HVOF Sprayed and Laser Cladded Stellite 6 Coatings Wear Behaviour (16.-18.06.2014)
6. F. Luo, A. Cockburn, R. Lupoi, M. Sparkes, and W. O'Neill, Performance Comparison of Stellite 6® Deposited on Steel Using Supersonic Laser Deposition and Laser Cladding, *Surf. Coat. Technol.*, 2012, **212**, p 119–127. https://doi.org/10.1016/j.surfcoat.2012.09.031
7. R. Singh, D. Kumar, S. Mishra, and S. Tiwari, Laser Cladding of Stellite 6 on Stainless Steel to Enhance Solid Particle Erosion and Cavitation Resistance, *Surf. Coat. Technol.*, 2014, **251**, p 87–97. https://doi.org/10.1016/j.surfcoat.2014.04.008
8. E. Toyserkani, S. Corbin, and A. Khajepour, *Laser Cladding*, CRC Press, Boca Raton, FL, 2005

9. Deloro Wear Solutions GmbH, Stellite 6 Alloy: Technical Data

10. R. Paes and A. Scheid, Effect of Deposition Current on Microstructure and Properties of CoCrWC Alloy PTA Coatings, *Soldagem Inspeção*, 2014, **19**(3), p 247–254. https://doi.org/10.1590/0104-9224/SI1903.07

11. M. Alimardani, V. Fallah, A. Khajepour, and E. Toyserkani, The Effect of Localized Dynamic Surface Preheating in Laser Cladding of Stellite 1, *Surf. Coat. Technol.*, 2010, **204**(23), p 3911–3919. https://doi.org/10.1016/j.surfcoat.2010.05.009

12. S. Sun, Y. Durandet, and M. Brandt, Parametric Investigation of Pulsed Nd: YAG Laser Cladding of Stellite 6 on Stainless Steel, *Surf. Coat. Technol.*, 2005, **194**(2–3), p 225–231. https://doi.org/10.1016/j.surfcoat.2004.03.058

13. Y. Cao, S. Zhu, X. Liang, and W. Wang, Overlapping Model of Beads and Curve Fitting of Bead Section for Rapid Manufacturing by Robotic MAG Welding Process, *Robot. Comput. Integr. Manuf.*, 2011, **27**(3), p 641–645. https://doi.org/10.1016/j.rcim.2010.11.002

14. S. Suryakumar, K.P. Karunakaran, A. Bernard, U. Chandrasekhar, N. Raghavender, and D. Sharma, Weld Bead Modeling and Process Optimization in Hybrid Layered manufacturing, *Comput. Aided Des.*, 2011, **43**(4), p 331–344. https://doi.org/10.1016/j.cad.2011.01.006

15. J. Xiong, G. Zhang, H. Gao, and L. Wu, Modeling of Bead Section Profile and Overlapping Beads with Experimental Validation for Robotic GMAW-Based Rapid Manufacturing, *Robot. Comput. Integr. Manuf.*, 2013, **29**(2), p 417–423. https://doi.org/10.1016/j.rcim.2012.09.011

16. A. Frenk, N. Henchoz, and W. Kurz, Laser Cladding of a Cobalt-Based Alloy: Processing Parameters and Microstructure, *Z. Met.*, 1993, **84**, p 886–892

17. A. Frenk and W. Kurz, High Speed Laser Cladding: Solidification Conditions and Microstructure of a Cobalt-Based Alloy, *Mater. Sci. Eng. A*, 1993, **173**(1–2), p 339–342. https://doi.org/10.1016/0921-5093(93)90240-F

18. Y.P. Kathuria, Some Aspects of Laser Surface Cladding in the Turbine Industry, *Surf. Coat. Technol.*, 2000, **132**(2–3), p 262–269. https://doi.org/10.1016/S0257-8972(00)00735-0

19. J.L. de van Mol Otterloo, and J. de Hosson, Microstructural Features and Mechanical Properties of a Cobalt-Based Laser Coating, *Acta Mater.*, 1997, **45**(3), p 1225–1236. https://doi.org/10.1016/S1359-6454(96)00250-9

20. M. Zhong, W. Liu, K. Yao, J.-C. Goussain, C. Mayer, and A. Becker, Microstructural Evolution in High Power Laser Cladding of Stellite 6 + WC Layers, *Surf. Coat. Technol.*, 2002, **157**(2–3), p 128–137. https://doi.org/10.1016/S0257-8972(02)00165-2

21. A.S.C. D'Oliveira, P.S.C. da Silva, and R.M. Vilar, Microstructural Features of Consecutive Layers of Stellite 6 Deposited by Laser Cladding, *Surf. Coat. Technol.*, 2002, **153**(2–3), p 203–209. https://doi.org/10.1016/S0257-8972(01)01687-5

22. R. Paes, D. Martinazzi, T. Falcade, and A. Scheid, Effect of Bead Overlapping on the Microstructure and Mechanical Properties of CoCrWC Alloy Coatings, *Mater. Res.*, 2018, **6**, p 157–163. https://doi.org/10.1590/1980-5373-MR-2018-0274

23. TUPY S.A, Certificado de ensaio: FUCO® FC 300 - Ferro Cinzento Pelítico

24. Bruker Corporation, E-mail correspondence (06.01.2021)

25. ASTM, Standard Test Methods for Determining Average Grain Size, 2013. https://doi.org/10.1520/E0112-12

26. Deutsches Institut für Normung e. V., Metallic Materials: Brinell Hardness Test—Part 1: Test Method (02.2015)

27. DIN Deutsches Institut für Normung e. V., Metallic Materials: Conversion of Hardness Values (02.2014)

28. Deutsches Institut für Normung e. V., Metallic Materials: Vickers Hardness Test—Part 1: Test Method (07.2018)

29. B. Haldar and P. Saha, Identifying Defects and Problems in Laser Cladding and Suggestions of Some Remedies for the Same, *Mater. Today Proc.*, 2018, **5**(5), p 13090–13101. https://doi.org/10.1016/j.matpr.2018.02.297

30. V. Ocelík, U. Oliveira, M. Boer, and J. Hosson, Thick Co-Based Coating on Cast Iron by Side Laser Cladding: Analysis of Processing Conditions and Coating Properties, *Surf. Coat. Technol.*, 2007, **201**(12), p 5875–5883. https://doi.org/10.1016/j.surfcoat.2006.10.044

31. H. El-Cheikh, B. Courant, S. Branchu, J.-Y. Hascoët, and R. Guillén, Analysis and Prediction of Single Laser Tracks Geometrical Characteristics in Coaxial Laser Cladding Process, *Opt. Lasers Eng.*, 2012, **50**, p 413–422. https://doi.org/10.1016/j.optlaseng.2011.10.014

32. T. Abioye, D. McCartney, and A. Clare, Laser cladding of Inconel 625 wire for corrosion protection, *J. Mater. Process. Technol.*, 2015, **217**, p 232–240. https://doi.org/10.1016/j.jmatprotec.2014.10.024

33. F. Arias-González, J. del Val, R. Comesaña, J. Penide, F. Lusquiños, F. Quintero, A. Riveiro, M. Boutinguiza and J. Pou, Fiber Laser Cladding of Nickel-Based Alloy on Cast Iron, *Appl. Surf. Sci.*, 2016, **374**, p 197–205. https://doi.org/10.1016/j.apsusc.2015.11.023

34. O. Nenadl, V. Ocelík, A. Palavra, and J. Hosson, The Prediction of Coating Geometry from Main Processing Parameters in Laser Cladding, *Phys. Procedia*, 2014, **56**, p 220–227. https://doi.org/10.1016/j.phpro.2014.08.166

35. A. Pinkerton, Advances in the Modeling of Laser Direct Metal Deposition, *J. Laser Appl.*, 2015, **27**(S1), p 1–8. https://doi.org/10.2351/1.4815992

36. U. Oliveira, V. Ocelík, and J. Hosson, Analysis of Coaxial Laser Cladding Processing Conditions, *Surf. Coat. Technol.*, 2005, **197**(2–3), p 127–136. https://doi.org/10.1016/j.surfcoat.2004.06.029

37. K. Bobzin, *Oberflächentechnik für den Maschinenbau*, Wiley, Hoboken, 2013. (**in German**)

38. W.C. Lin and C. Chen, Characteristics of Thin Surface Layers of Cobalt-Based Alloys Deposited by Laser Cladding, *Surf. Coat. Technol.*, 2006, **200**(14–15), p 4557–4563

39. E. Hug, C. Keller, P.-A. Dubos, and M.M. Celis, Size Effects in Cobalt Plastically Strained in Tension: Impact on Gliding and Twinning Work Hardening Mechanisms, *J. Mater. Res.*, 2021, **11**, p 1362–1377. https://doi.org/10.1016/j.jmrt.2021.01.105

40. M. Lachowicz, K. Haimann, W. Dudzinski, M. Morawska-Sołtysik, ARCHIVES 10/3 Characteristic of Intermetallic Phases in Cast Dental CoCrMo Alloy, Archives of Foundry Engineering 10

41. S.M. Gaytan, L.E. Murr, D.A. Ramirez, B.I. Machado, E. Martinez, D.H. Hernandez, J.L. Martinez, F. Medina, and R.B. Wicker, A TEM Study of Cobalt-Base Alloy Prototypes Fabricated by EBM, *Mater. Sci. Appl.*, 2011, **2**(5), p 355–363. https://doi.org/10.4236/msa.2011.25046

42. L. Rémy and A. Pineau, Twinning and Strain-Induced f.c.c. → h.c.p. Transformation on the Mechanical Properties of CoNiCrMo Alloys, *Mater. Sci. Eng.*, 1976, **26**(1), p 123–132. https://doi.org/10.1016/0025-5416(76)90234-2

43. X. Wu, N. Tao, Y. Hong, G. Liu, B. Xu, J. Lu, and K. Lu, Strain-Induced Grain Refinement of Cobalt During Surface Mechanical Attrition Treatment, *Acta Mater.*, 2005, **53**(3), p 681–691. https://doi.org/10.1016/j.actamat.2004.10.021

44. P. Chowdhury, H. Sehitoglu, W. Abuzaid, and H.J. Maier, Mechanical Response of Low Stacking Fault Energy CoNi Alloys—Continuum, Mesoscopic and Atomic Level Treatments, *Int. J. Plast.*, 2015, **71**, p 32–61. https://doi.org/10.1016/j.ijplas.2015.04.003

45. A. Gholipour, M. Shamanian, and F. Ashrafizadeh, Microstructure and Wear Behavior of Stellite 6 Cladding on 17–4 PH Stainless Steel, *J. Alloys Compd.*, 2011, **509**(14), p 4905–4909. https://doi.org/10.1016/j.jallcom.2010.09.216

46. F. Rosalbino and G. Scavino, Corrosion Behaviour Assessment of Cast and HIPed Stellite 6 Alloy in a Chloride-Containing Environment, *Electrochim. Acta*, 2013, **111**, p 656–662. https://doi.org/10.1016/j.electacta.2013.08.019

47. B. Venkatesh, K. Sriker, and V. Prabhakar, Wear Characteristics of Hardfacing Alloys: State-of-the-art, *Procedia Mater. Sci.*, 2015, **10**, p 527–532. https://doi.org/10.1016/j.mspro.2015.06.002

48. J. Sort, S. Suriñach, J.S. Muñoz, M.D. Baró, M. Wojcik, E. Jedryka, S. Nadolski, N. Sheludko, and J. Nogués, Role of Stacking Faults in the Structural and Magnetic Properties of Ball-Milled Cobalt, *Phys. Rev. B*, 2003, **68**, p 1. https://doi.org/10.1103/PhysRevB.68.014421

49. E. Abouda, M. Dal, P. Aubry, T. Tarfa, I. Demirci, C. Gorny, and T. Malot, Effect of Laser Cladding Parameters on the Microstructure and Properties of High Chromium Hardfacing Alloys, *Phys. Procedia*, 2016, **83**, p 684–696. https://doi.org/10.1016/j.phpro.2016.08.070

50. T. Antoszczyszyn, R. Paes, A. Oliveira, and A. Scheid, Impact of Dilution on the Microstructure and Properties of Ni-Based 625 Alloy Coatings, *Soldagem Inspeção*, 2014, **19**(2), p 134–144. https://doi.org/10.1590/0104-9224/SI1902.05

51. J. De Hosson and J. De Mol Van Otterloo, Microstructural Features and Mechanical Properties of a Cobalt-Based Laser Coating, *Acta Mater.*, 1997, **45**(3), p 1225–1236

52. M. Ferozhkhan, M. Duraiselvam, K. Kumar, and R. Ravibharath, Plasma Transferred Arc Welding of Stellite 6 Alloy on Stainless Steel

for Wear Resistance, *Procedia Technol.*, 2016, **25**, p 1305–1311. h ttps://doi.org/10.1016/j.protcy.2016.08.226

53. A. d'Oliveiraa, P. da Silvaa, and R. Vilarc, Microstructural Features of Consecutive Layers of Stellite 6 Deposited by Laser Cladding, *Surf. Coat. Technol.*, 2002, **153**, p 203–209

54. D. Karmakar, M. Gopinath, S. Harmalkar, and A. Nath, Investigation of Wear and Corrosion Characteristics of Stellite-6 and Stellite-21 Layers Deposited by Co-axial Laser Cladding, *Proceedings of the ASME 2017 12th International Manufacturing Science and Engineering Conference*, ASME, 2017, p 1–6

55. A. Kusmoko, D. Dunne, H. Li, and D. Nolan, Effect of Two Different Energy Inputs for Laser Cladding of Stellite 6 on P91 and P22 Steel Substrates, *Procedia Mater. Sci.*, 2014, **6**, p 26–36. https://doi.org/10.1016/j.mspro.2014.07.005

56. A. Farnia, F. Malek Ghaini, V. Ocelík, and J. Hosson, Microstructural Characterization of Co-based Coating Deposited by Low Power Pulse Laser Cladding, *J. Mater. Sci.*, 2013, **48**(6), p 2714–2723. https://doi.org/10.1007/s10853-012-7069-8

57. A. Kusmoko, D. Dunne, and H. Li, Effect of Heat Input on Stellite 6 Coatings on a Medium Carbon Steel Substrate by Laser Cladding, *Mater. Today Proc.*, 2015, **2**, p 1747–1754. https://doi.org/10.1016/j.matpr.2015.07.010

58. A. Kumar and S. Roy, Effect of Three-Dimensional Melt Pool Convection on Process Characteristics During Laser Cladding, *Comput. Mater. Sci.*, 2009, **46**(2), p 495–506. https://doi.org/10.1016/j.commatsci.2009.04.002

59. G. Schulze, *Die Metallurgie des Schweissens: Eisenwerkstoffe - nichteisenmetallische Werkstoffe*, 4th ed. VDI-Buch, Springer, Heidelberg, 2010. (**in German**)

60. J.-M. Jouvard, D. Grevey, F. Lemoine, and A. Vannes, Continuous Wave Nd:YAG Laser Cladding Modeling: A Physical Study of Track Creation During Low Power Processing, *J. Laser Appl.*, 1997, **9**, p 43–50

61. D.M. Goodarzi, J. Pekkarinen, and A. Salminen, Effect of Process Parameters in Laser Cladding on Substrate Melted Areas and the Substrate Melted Shape, *J. Laser Appl.*, 2015, **27**(S2), p S29201. h ttps://doi.org/10.2351/1.4906376

62. S. Wen, Y. Shin, J. Murthy, and P. Sojka, Modeling of Coaxial Powder Flow for the Laser Direct Deposition Process, *Int. J. Heat Mass Transf.*, 2009, **52**(25–26), p 5867–5877. https://doi.org/10.1016/j.ijheatmasstransfer.2009.07.018

63. R. Jendrzejewski, G. Śliwiński, M. Krawczuk, and W. Ostachowicz, Temperature and Stress Fields Induced During Laser Cladding, *Comput. Struct.*, 2004, **82**(7–8), p 653–658. https://doi.org/10.1016/j.compstruc.2003.11.005

64. W. Betteridge, *Cobalt and Its Alloys*, Horwood and Wiley, Chichester, 1982

65. A. Karl, P. Schaaf, J. Bergmann, and A. Dwars, *Laserauftragschweißen hochlegierter Duplexstähle, Vol. 10 of Werkstofftechnik aktuell*, Univ.-Bibliothek and Univ.-Verl. Ilmenau, Ilmenau, 2014. (**in German**)

66. J. Lippold, *Welding Metallurgy and Weldability*, Wiley, Hoboken, 2015. https://doi.org/10.1002/9781118960332

67. P. Sahm Ed., *Schmelze, Erstarrung, Grenzflächen: Eine Einführung in die Physik und Technologie flüssiger und fester Metalle*, Vieweg, Braunschweig, 1999 (**in German**)

68. A. Frenk and W. Kurz, Microstructural Effects on the Sliding Wear Resistance of a Cobalt-Based Alloy, *Wear*, 1994, **174**, p 81–91

69. H. Berns Ed., *Hartlegierungen und Hartverbundwerkstoffe: Gefüge, Eigenschaften, Bearbeitung, Anwendungen*, Springer, Berlin, 1998 (**in German**)

70. H. Kleykamp, Thermodynamic Studies on Chromium Carbides by the Electromotive Force (emf) Method, *J. Alloys Compd.*, 2001, **321**(1), p 138–145. https://doi.org/10.1016/S0925-8388(01)01012-X

71. S. Du Sichen and L.-I. Sheetharaman, Staffansson, Standard Gibbs Energies of Formation of the Carbides of Chromium by emf Measurements, *Metall. Mater. Trans. B*, 1989, **20**(6), p 911–917. h ttps://doi.org/10.1007/BF02670196